The Astrophysical Journal, 921:81 (14pp), 2021 November 1 https://doi.org/10.3847/1538-4357/ac178f

The Young Stellar Population, Distance, and Cloud–Cloud Collision Induced Star Formation Scenario of the Trifid Nebula

Venu M. Kalari[1,2]
[1] Gemini Observatory/NSFs NOIRLab, Casilla 603, La Serena, Chile; vkalari@gemini.edu
[2] Departamento de Astronomia, Universidad de Chile, Casilla 36-D, Santiago, Chile
Received 2021 April 13; revised 2021 July 15; accepted 2021 July 16; published 2021 November 2

Abstract

The Trifid Nebula is a young, nearby star-forming region where star formation is proposed to have been triggered by cloud–cloud collision (CCC), based on observations of molecular clouds. It offers a unique opportunity to test whether the CCC hypothesis is supported by the spatial distribution and star formation chronology of young stars. We present the first study of the optically visible pre-main sequence (PMS) population of the region using *ri*Hα imaging and Gaia astrometry. Combined with an analysis of young stellar objects (YSOs) using infrared imaging, we capture the spatial distribution and star formation chronology of the young stellar population. From the analysis, 15 Flat/Class I YSOs, 46 Class II YSOs, and 41 accreting PMS stars are identified (diskless/non-accreting sources are not included in the analysis). The distance based on Gaia parallaxes is ∼1250 pc, significantly closer than previously reported. The Class II YSOs and PMS stars (∼1.5 Myr old) are spread toward the edge of the molecular clouds. They are slightly younger than the estimated crossing time of ∼2.7 Myr and closer to the estimated dynamical age ∼0.85 Myr. Younger Class I YSOs are more concentrated spatially. There exists a cavity devoid of young stars where the two clouds overlap. This evidence suggests that the current generation of stars formed after the collision of two clouds ∼1 Myr ago, and this result can be corroborated using future spectroscopic studies.

Unified Astronomy Thesaurus concepts: Star formation (1569); Star forming regions (1565); H II regions (694); Young stellar objects (1834); Pre-main sequence stars (1290)

Supporting material: machine-readable tables

1. Introduction

There remain many open questions in the field of star formation. In the current paradigm, star formation is a dynamical process, occurring primarily as a result of gravitational instabilities seeded by turbulence in molecular clouds (McKee & Ostriker 2007). A spectacular trigger for gravitational instabilities and the eventual collapse of molecular clouds into stars is cloud–cloud collision (CCC). It is has been argued that the collision of one or more molecular clouds can potentially cause overdensities, leading to gravitational collapse and subsequent star formation (Loren 1976). Recent observations at submillimeter wavelengths have presented evidence that CCC is a viable mechanism to form stars and young clusters across the Milky Way and in external galaxies (Fukui et al. 2021).

The young star-forming region Trifid Nebula (or M20, NGC 6514) is a proposed site of CCC induced star formation (Torii et al. 2011, 2017), based on the systemic velocities and masses of two molecular clouds in the region. These two clouds are thought to have collided ∼1 Myr ago, producing the young stellar population observed in the region. M20 is one of the youngest sites (∼0.3–1 Myr; Rho et al. 2008) proposed to have formed via CCC. It is thought to lie between 1.6 and 2.7 kpc (Rho et al. 2008; Cambrésy et al. 2011), in either the Sagittarius or Scutum arm, respectively. This combination of proximity and age allows one to observe and characterize the young low-mass stellar population of the region, a possibility not afforded in studies of more distant sites of CCC (Fukui et al. 2021). It is therefore an ideal avenue to gauge whether the young stellar population is supportive of an induced star formation scenario.

The stellar population of the region has not been studied in the optical. An O7.5V star, HD 164492A (with a spectroscopic age of 0.6 Myr; Petit et al. 2019), ionizes the optically observed nebula (see Figure 1) and lies southwest of the crux of the three bisecting dust lanes. The extinction law in the region is anomalous at $R_V = 5.5$ (Cambrésy et al. 2011). The combination of nebulosity, extinction, and a line of sight toward the Galactic plane has hindered optical observations. Although there have been no optical studies of the young stellar population in the region, multiple studies at radio, submillimeter, mid-infrared (MIR), and near-infrared (NIR wavelengths) have been conducted (Yusef-Zadeh et al. 2000; Rho et al. 2001, 2006, 2008; Lefloch et al. 2002; Feigelson et al. 2013). These studies have revealed a rich young stellar population at a very nascent stage of star formation ($\lesssim$1 Myr old), a population of even younger star-forming cores (Tapia et al. 2018), and evidence for photoionization affecting ongoing star formation (Yusef-Zadeh et al. 2005).

The different wavelengths trace the varying stages of ongoing star formation in the region: from the molecular clouds visible at submillimeter and radio wavelengths to the young protostars in the infrared (IR). Studies of the optically visible pre-main sequence (PMS) stars and the stellar cluster would complete the circle, helping to piece together the star formation picture. With a combination of deep optical photometry and astrometry from the Gaia space telescope, it is now possible to both observe the low-mass optically visible PMS stars and disentangle them from the line of sight of contaminants. Thus, when combined with archival IR data, we are now armed with observations to characterize the young stellar population of the Trifid Nebula and examine how they relate to the proposed CCC triggered star formation scenario.

In this paper we identify and characterize the young stellar population in the Trifid Nebula using IR and optical observations, combined with Gaia astrometry, to investigate whether the

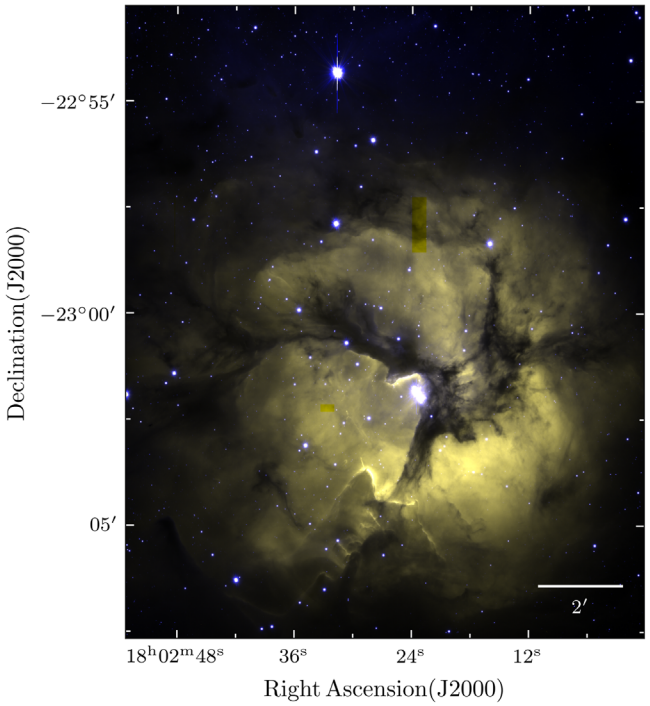

Figure 1. The Trifid Nebula as an *rgb* image from VPHAS+ *i*, Hα, and *r* images, respectively. The area shown is centered on right ascension (J2000) $18^h02^m26^s8$ and declination (J2000) −23°00′12″, with a field of view 12′ 2 × 14′9, and covers the area studied in this work. North is up and east to the left. The central ionizing O7.5V star in the HD 164492 system is visible as the bright central star. Nebulosity, varying on small spatial scales, is also seen.

triggered star formation scenario proposed in the literature can explain the observed spatial distribution and star formation chronology of the young stellar population. This paper is organized as follows: In Section 2, a description of the data used in this work is presented. Sections 3 and 4 describe the identification and classification of the IR young stellar population and optically visible PMS stars, respectively. In Section 5 a discussion on the star formation scenario in the Trifid Nebula is presented.

2. Data

2.1. Area of Study

To identify and characterize the young stellar population in the star-forming region M20, we define our area of study as all sources falling within a bounding box of 12′2 × 14′9 region centered on right ascension $18^h02^m26^s8$ and declination −23° 00′12″ (see Figure 1). The area definition is slightly smaller than previous studies at NIR or X-ray wavelengths (Rho et al. 2001, 2006; Feigelson et al. 2013) and completely includes only the central Trifid Nebula and the blister region located immediately above it. Because M 20 lies directly in our line of sight toward the Galactic plane, multiple populations in farther arms will be confused with optical members. The optical nebulosity as seen in M 20 can prevent the detection of more distant contaminants in the plane, providing an upper blue envelope in the color–magnitude diagram. In addition, the area chosen adequately covers the region where CCC and subsequent star formation are thought to have occurred (Torii et al. 2011). Choosing a slightly larger area of study while potentially enabling a more detailed understanding of the extent of the region will include more distant non-members that cannot be separated easily, justifying our choice of boundaries.

2.2. *VPHAS+* ugri*H*α *Imaging*

The VPHAS+ (VST/Omegacam Photometric Hα Survey of the Southern galactic plane and bulge) survey observed the Trifid Nebula in *ugri*Hα filters and is comprehensively outlined in the survey paper by Drew et al. (2014). The data used in this publication are part of the VPHAS+ third data release. The reader is referred to the release document[3] for details of the data reduction procedure. An *rgb* image created using the final reduced images is shown in Figure 1 to illustrate the quality of the imaging and the area studied in this work. Clearly visible are the three central dust lanes and the photoionized regions toward the south.

Aperture photometry was performed on these reduced images using a dedicated pipeline run by the Cambridge Astronomy Survey Unit. Attention is drawn to the dedicated software *nebuliser* used in the photometric pipeline to track variable background emission on a sliding scale around 15″. Objects that suffer from improper background subtraction due to rapidly varying nebulosity on smaller scales are flagged using a curve-of-growth analysis as possibly non-stellar. The final catalog available from the archive is calibrated in the AB magnitude system. A global Vega magnitude calibration is achieved across all filters by cross-matching sources overlapping with the VPHAS+ DR2 data, which were globally calibrated on the Vega magnitude scale. The global shifts are 1.084, −0.055, 0.138, 0.461, and 0.316 in *ugri*Hα filters, respectively. For the remainder of the study, the magnitudes reported are in the Vega magnitude scale.

From the publicly available catalog, we select all sources falling within the area of interest. We apply further selection criteria of (i) $r > 13$ to remove saturated sources, (ii) photometric uncertainties in *ri* less than 0.1 mag and in Hα less than 0.15 mag to keep low propagated errors, and (iii) sources classified as stellar or star-like in broadband *ri* photometry to remove extended objects. For Hα photometry, mild degradation of the point-spread function may lead to spurious classifications as extended objects. To avoid this and not reject acceptable Hα measurements, the classification in Hα is relaxed to extended sources. Instead, a further visual check using unsharp masking on selected sources is imposed to eliminate any sources affected by sharply varying nebulosity (see Kalari et al. 2015), (iv) sources with average photometric confidence greater than 90 to remove sources falling in the chip gaps. Note that we do not impose any quality criteria on *ug* photometry. The cleaned sample contains 9227 unique sources with *ri*Hα photometry meeting the quality criteria. The color–magnitude diagram generated using the data is shown in Figure 2. The saturation limit of VPHAS+ photometry means that the bright, early-type members of the Trifid Nebula are missing from our analysis. Unlike other nearby star-forming regions near the Galactic plane, there is no upper blue envelope owing to the nebulosity. More distant Galactic contaminants are visible, particularly at the edges of the nebula.

Finally, a result of our selection criteria is that stars near the nebulous center and along the dust lanes are preferentially removed, as they lie along regions of very rapidly spatially varying nebulosity. Optical photometry from the Gaia telescope

[3] http://www.eso.org/rm/api/v1/public/releaseDescriptions/106

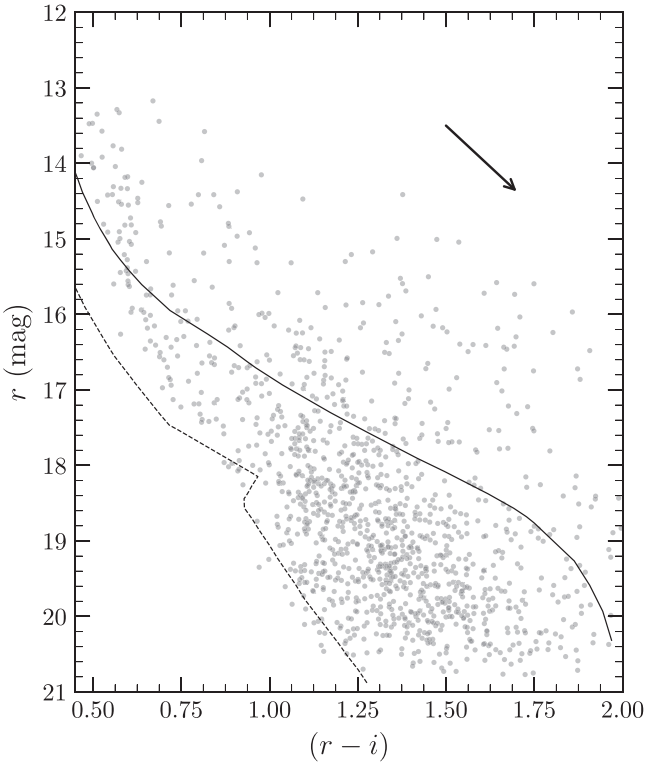

Figure 2. Observed ($r-i$) vs. r color–magnitude diagram of all sources studied in this work. A reddening vector of $A_V = 1$ mag, $R_V = 5.5$ is shown in the upper right corner. Bressan et al. (2012) isochrones of 1 (solid) and 10 Myr (dashed) at a distance of 1250 pc and $A_V = 1.3$ mag are shown.

also shows similar spatial density to the VPHAS+ observations, suggesting that observations at the optical wavelength toward the central region suffer greatly from the spatial varying nebulosity. The consequences of this spatial density variation in the optical on our results are discussed in Section 4.6.

2.3. Gaia EDR 3 Astrometry

Astrometric data from the Gaia early data release 3 (EDR3; Gaia Collaboration et al. 2020) are cross-matched to the VPHAS+ data. Gaia EDR3 data contain parallaxes (π), proper-motion vectors in right ascension ($\mu_\alpha \cos\delta$, hereafter referred to as μ_α), declination (μ_δ), and the associated photometry in custom filters measured from the first 3 yr of Gaia observations (2014–2017) in the 2016 reference epoch. Gaia EDR3 photometry has a detection threshold of $G \sim 21$ mag, with the very bright ($G < 7$ mag) and high-proper-motion ($>0\farcs6\,\mathrm{yr}^{-1}$) stars incomplete. The detection limit of Gaia corresponds approximately to the 3σ threshold of the VPHAS+ photometry in the *ri* filters. Errors in EDR3 data release on the proper motions are believed to be around $\pm$ 0.02–1.4 mas depending on source magnitude, and on parallax around $\pm$0.02–1.3 mas. A comparison with extragalactic sources indicates an overall negative bias of -17 μas (Gaia Collaboration et al. 2020) on the parallax, which was added to our parallax measurements.

To perform cross-matching with the VPHAS+ sample, a minimum cross-match radius of $0\farcs1$ was set considering the Gaia positional accuracy ($0\farcs059$) and separation between the different epochs (also $0\farcs059$). Sources were initially matched using a maximum radius of $2''$ (with both catalogs in the J2000 epoch), where the mean separation was found to be $0\farcs077$. To determine the incidence of spurious sources, the radius was incrementally reduced by $0\farcs05$, while also counting the number of stars with magnitude differences between the Gaia G band, and the VPHAS+ i magnitude (applying an offset of 0.6 mag to bring approximately to a relation of unity) was greater than 1 mag (accounting for variability; note that r band is not used, as it includes the Hα line). A best-match radius of $0\farcs3$ is chosen, as 98% of matches within $1''$ are recovered, but no sources with large magnitude offsets are picked up. The renormalized unit weight error (RUWE) cut of RUWE < 1.4 was applied to remove sources with poor astrometry. As a result, 8965 sources with high-fidelity astrometry and photometry from Gaia EDR3 that have cross-matches in VPHAS+ compose our data set. This is the data set that will be utilized for identifying and characterizing the young stellar population visible at optical wavelengths.

2.4. NIR and MIR Imaging

The NIR sample consists of all sources with *JHK*s photometry from the UKIDSS (UKIRT Infrared Deep Sky Survey; Lucas et al. 2008) survey. For this sample, we discarded sources with non-stellar profiles (akin to the classification schema in the VPHAS+ photometry), or lacking photometry in any of the three bands, but applied no further selection criteria. This catalog is cross-matched with the VPHAS+–Gaia sample. Given the detection limit of UKIDSS ($\sim$19.7 mag in J), the optical sample misses some of the lower-mass mid-M spectral type stars (assuming average extinction, with no impact of nebulosity) that are captured by the NIR photometry. However, nebulosity toward the core of the Trifid Nebula greatly impacts our detection of sources in the region. The effect of this incompleteness in optical photometry compared to the NIR on our final results is discussed in further detail in Section 4.6.

To capture the disk evolutionary stages using data from the MIR, we utilize archival photometry from the GLIMPSE (The Galactic Legacy Infrared Midplane Survey Extraordinaire; Benjamin et al. 2003) survey catalog. GLIMPSE details photometry in the [3.6], [4.5], [5.8], and [8.0] IRAC (InfraRed Array Camera) filters along the Galactic plane, taken using the Spitzer space telescope. Only sources with no close sources within $2''$ and with no photometric quality issue considered. No photometric uncertainty limit was applied to the data set. To this sample, we performed a cross-match search against the MIPSGAL survey (MIPS Galactic Plane Survey; Urquhart et al. 2014) to find any sources having photometry at 24 μm, which was taken using the MIPS (Multiband Imaging Photometer for Spitzer) instrument. Note that both the MIR catalogs already contain cross-matches to the Two Micron All Sky Survey *JHK*s (Cutri et al. 2003) photometry catalog. We cross-match the MIR catalog with the UKIDSS and VPHAS+–Gaia data sets using a radius of $2''$ (the mean effective resolution of the MIR photometry), and we performed a sanity check on the cross-matches by removing any sources that have GLIMPSE provided *K*s-band photometry deviant by more than 0.5 mag from the UKIDSS survey *K*s photometry.

3. Young Stellar Objects

Young stellar objects (YSOs) may be discriminated from the stellar population on the basis of their IR properties. Depending on their evolutionary stage, YSOs are likely to be surrounded by either circumstellar disks or envelopes that absorb and

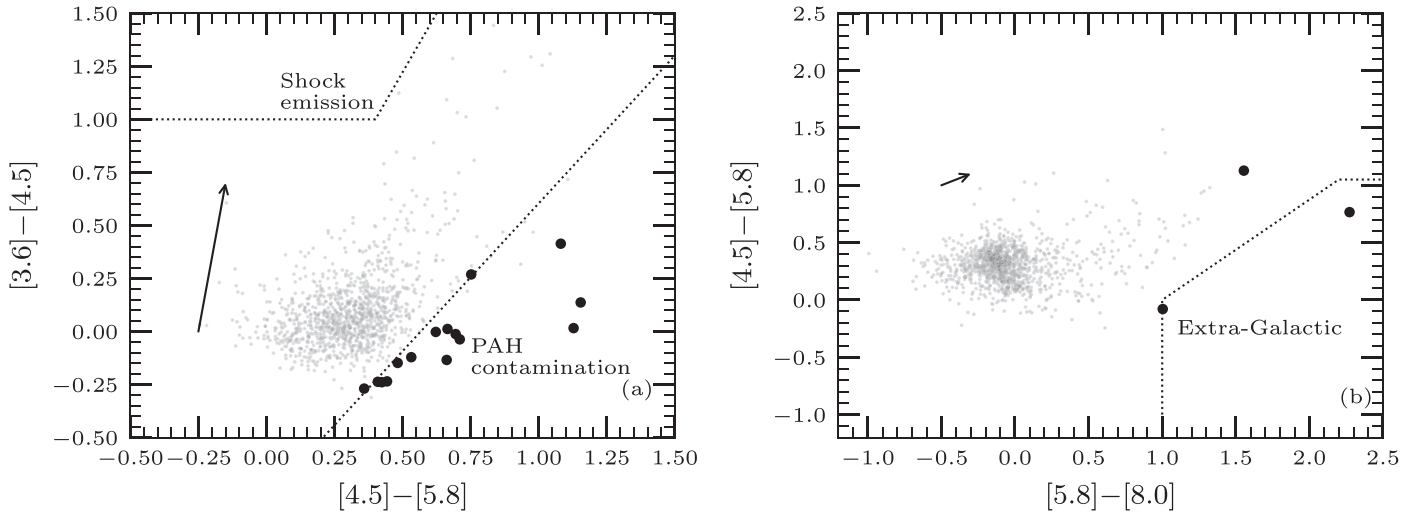

Figure 3. (a) [4.5]−[5.8] vs. [3.6]−[4.5] color–color diagrams of all MIR sources are shown as circles. The locations of sources affected by PAH contamination and shock emission are shown following Gutermuth et al. (2009). Stars removed following the criteria outlined in the text as contaminated photometry are marked by filled circles. (b) [5.8]−[8.0] vs. [4.5]−[5.8] color–color diagrams of all sources are shown. Sources that are probable external galaxies following Gutermuth et al. (2009) classification criteria are marked by filled circles. The reddening vector for $A_K = 5$ mag is also shown. The MIR reddening law of Indebetouw et al. (2005) was used.

re-radiate stellar luminosity in the IR portion of the electromagnetic spectrum. At these wavelengths, the colors of YSOs and the shape of their spectral energy distribution (SED) significantly differ with respect to the vast majority of observable stars. The database of NIR and MIR photometry spanning the wavelength range of 1.25–24 μm described in Section 2.4 is used to both identify YSOs and classify their evolutionary stage in this section.

3.1. Identification of Young Stellar Objects

To identify probable YSOs, we select from the Spitzer IRAC sample only sources with photometry in all four bands. In addition, NIR and 24 μm photometry of these sources is also used for the analysis when available. The main source of contamination when attempting to identify YSOs against the Galactic plane is dealing with foreground/background stars and polycyclic aromatic hydrocarbon (PAH) and background galaxies. Most foreground/background stars do not have IR excesses and are centered around zero in Spitzer color–color planes (Megeath et al. 2004). Removal of asymptotic giant branch (AGB) stars is less straightforward, as they do exhibit excesses similar to YSOs in some IR colors. Similarly, background galaxies have colors falling in the region occupied by YSOs in the MIR color–color plane. Active star-forming galaxies in particular have colors that are dominated by PAH emission, and they are bright in the [8.0] filter (due to the 7.7–8.2 μm PAH feature). Active galactic nuclei (AGNs) are similarly bright at 8 μm and also overlap YSOs in the color–color plane. In addition, the photometry also may be affected by unresolved knots caused by shock emission from YSOs, or from PAH emission contaminating the apertures of sources. The latter two represent significant sources of photometric contamination in star-forming regions. To remove extragalactic sources and contaminated photometry, we adopt the criteria outlined in Gutermuth et al. (2009), Appendix A. Note that a reddening correction corresponding to an absolute extinction, A_V, of 1.3 mag (Rho et al. 2008), following the reddening law (R_V) of 5.5 (Cambrésy et al. 2011), was applied. The results of this exercise are shown in Figure 3. Overall, ∼20 sources were removed following these criteria. In addition, to identify stellar contaminants, a cutoff of ([4.5]−[8.0]) < 0.5 and [8.0] < 5 mag following Harvey et al. (2006) was applied. The cutoff in magnitude is scaled to a distance of 1250 pc (see Section 4.3 for details on the chosen distance). These sources are not removed from the sample immediately, but this cutoff is applied when classifying YSOs.

3.2. Classification of Young Stellar Objects

There exist multiple criteria outlined in the literature to identify and classify YSOs using either the value of the IR SED slope (α) or positions of sources in color–color diagrams. These methods are similar in philosophy but differ in details. A full review and examination of these criteria is beyond the scope of this paper, and we base the analysis in this paper on a combination of the color and slope classification criteria outlined in Megeath et al. (2004) and Allen et al. (2004) and in Harvey et al. (2006), respectively. First, we classify all sources that were not identified as extragalactic sources, or having photometry contaminated by PAH or shock emission using the value of α, defined as

$$\alpha = \frac{d \log \lambda F_\lambda}{d \log(\lambda)}. \quad (1)$$

Here λ is wavelength and λF_λ is flux density in wavelength. To determine α, we fit the fluxes of all sources longward of 2 μm. For all sources, we require at least photometry in all IRAC bands. The photometry was dereddened assuming the mean extinction toward the region. The slope was calculated using a weighted least-squares fit to the available photometry. Here, the weight applied was the inverse of the squared photometric errors. The fit error from a standard weighted least-squares fit is also calculated.

Following the classification scheme of Harvey et al. (2006), we classify sources as YSOs based on their α value. The YSO classes are as follows:

1. Class I: $\alpha > 0.3$.
2. Flat: $0.3 \geqslant \alpha \geqslant -0.3$.
3. Class II: $-0.3 > \alpha \geqslant -1.6$.

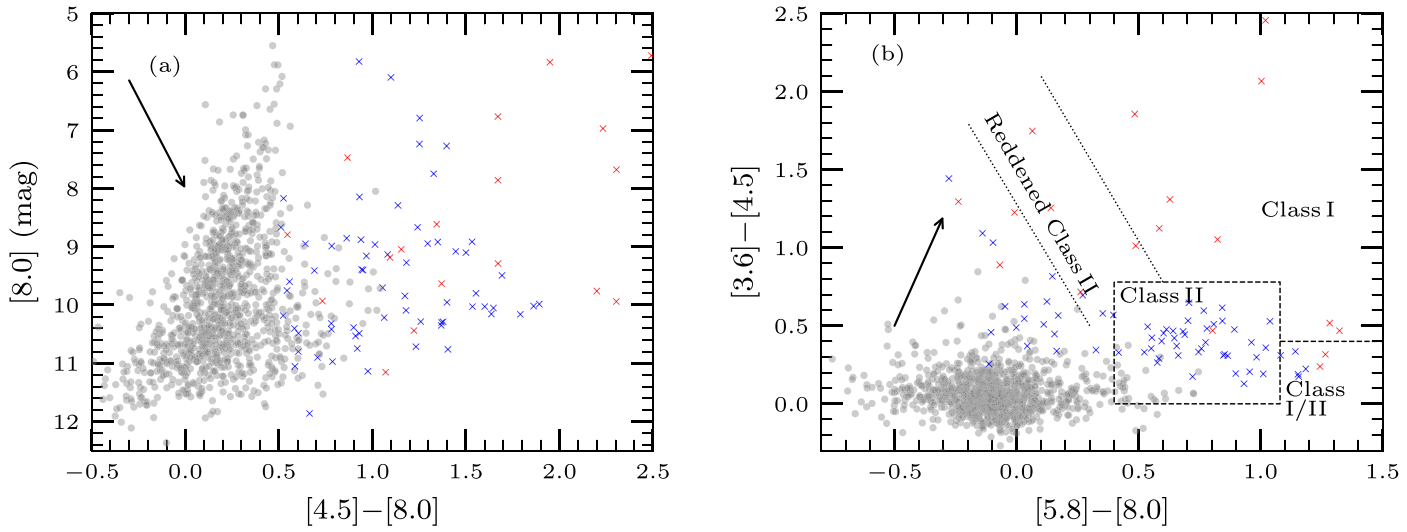

Figure 4. (a) [4.5]−[8.0] vs. [8.0] color–magnitude diagrams of MIR sources are shown as circles. Sources identified as Class I and Class II YSOs are marked as red and blue crosses, respectively. (b) [5.8]−[8.0] vs. [3.6]−[4.5] color–color diagrams of all sources. The locations of Class II and Class I sources following Allen et al. (2004) and Megeath et al. (2004) classification criteria are shown. The reddening vector for $A_K = 5$ mag is also shown, based on the Indebetouw et al. (2005) reddening law.

Note that we do not attempt to classify Class III sources. Class III sources (YSOs with no or transition disks) cannot be differentiated from the bulk of the stellar population, as they lack IR excesses. While in the literature Class III sources have been classified as non-contaminants with $\alpha < -1.6$, we refrain from doing so here because the Trifid Nebula lies in a direct sight line toward the Galactic plane, and even in MIR it is heavily contaminated by background/foreground field stars (Feigelson et al. 2013). Therefore, classifying Class III sources based on α would lead to spurious detections.

Spitzer images of the sources were visually inspected to detect any that may be affected by extended emission or nearby contaminating bright sources (recall that we discard previously any sources having counterparts within 2″, the mean FWHM of the photometry) or that are elongated. Three sources that are extended or have a nearby bright source within 2.″5 are removed. Note that the bulk of our sample has $\alpha \sim -2.5$ to -3, agreeing with the expectation for main-sequence stars.

After the SED slope analysis, an additional color selection is applied to cut any remaining contaminants (e.g., AGB stars, reddened main-sequence stars). The criteria outlined in Megeath et al. (2004) and Allen et al. (2004) are utilized, and the results are shown in Figure 4. Here, the approximate colors of Class II, Class I, a combination of Class I/II sources, and reddened Class II YSOs given by Megeath et al. (2004) and Allen et al. (2004) are shown. The locations of sources classified based on α are also shown. The loci of main-sequence sources without excess in the IR are centered around zero as expected, with a spread due to reddening differences and CO absorbing giants. The positions of Class II sources are demarcated by the bounding box, which is reproduced by models of disks with varying accretion rates and inclinations around young and low-mass stars (D'Alessio et al. 2001). The empirical boundary between Class II and Class I sources is also given, and their colors are of protostellar objects with infalling envelopes. The location of Class II sources affected by [8.0] excess emission is marked in the region of Class I/Class II sources, as is the location of Class II sources affected by extreme reddening. While, in general, the location of these sources agrees with the expectation based on their color criteria, we note that 17 sources fall blueward of the region demarcated as either Class II or reddened Class II sources. Sources falling in this location are spatially preferentially located toward the edges of the nebula, directly in the sight of the Galactic plane, and have colors ([4.5]−[8.0]) < 1 (Harvey et al. 2006), similar to AGB stars. These are likely reddened AGB stars in the Galactic plane. To remove them, these 17 sources falling outside of the expected color boundaries for YSOs from Megeath et al. (2004) and Allen et al. (2004) are removed.

3.3. Final Sample of YSOs

Our final sample consists of 46 Class II, 9 Flat, and 6 Class I YSOs. The complete sample, along with archival photometry, is given in Table 1. A source of contamination in our final sample is background/foreground AGB stars, as sources resembling colors of galaxies, or contaminated aperture photometry, were removed, and the images of the final classified sources were visually inspected. The contamination rate in our sample may be judged by adopting the locations of AGB stars in color–magnitude diagrams as found by Harvey et al. (2006). In that paper, it is suggested that some AGB stars that may have similar SED slopes to YSOs have colors ([4.5] −[8.0]) < 1. These AGB stars represent the largest source of contamination in our sample, given the sight line toward the Galaxy. Twelve YSOs have colors bluer than AGB stars (but redder than ([4.5]−[8.0]) > 0.5), and these represent ∼20% of our sample. This represents an upper limit on the estimate of the contamination in the sample, given that otherwise the sources meet the SED and color classification criteria.

The completeness of the sample is difficult to judge straightforwardly, as there are various factors affecting it, in particular, the saturation of photometry toward the center of the Trifid Nebula and the large-scale differences in the nebulosity. These cannot be straightforwardly estimated even using a control field given the location near the Galactic bulge. A similar conclusion was arrived at by the study of Feigelson et al. (2013), who identified YSOs in the Trifid Nebula based on a combination of modeling IR SEDs and X-ray emission.

Table 1
Infrared Photometry of Young Stellar Objects in the Trifid Nebula

GLIMPSE ID	J (mag)	H (mag)	Ks (mag)	[3.6] (mag)	[4.5] (mag)	[5.8] (mag)	[8.0] (mag)	α	Class
G006.9115-00.2629				12.07 ± 0.06	10.30 ± 0.04	9.26 ± 0.04	9.18 ± 0.09	1.02 ± 0.3	I
G006.9258-00.2629	13.27 ± 0.02	12.33 ± 0.02	11.73 ± 0.033	10.88 ± 0.05	10.55 ± 0.04	10.17 ± 0.06	9.08 ± 0.06	-0.9 ± 0.2	II
G006.9292-00.2460	16.30 ± 0.10	14.08 ± 0.05	12.13 ± 0.02	9.53 ± 0.03	8.46 ± 0.03	7.60 ± 0.03	6.76 ± 0.02	0.2 ± 0.1	Flat
G006.9451-00.3318		14.18 ± 0.07	12.45 ± 0.05	10.60 ± 0.17	10.00 ± 0.13	9.32 ± 0.04	8.96 ± 0.03	-1.49 ± 0.3	II
G006.9637-00.3104	11.15 ± 0.02	10.75 ± 0.02	10.42 ± 0.02	9.7 ± 0.08	9.23 ± 0.04	8.26 ± 0.082	6.97 ± 0.18	0.27 ± 0.4	Flat

Note. Five selected rows are shown to display the form and contents of the table. The full table is only available electronically, along with the source coordinates. The 24 μm magnitude is 1.7 ± 0.03 mag for G007.0317-00.2845, 2.29 ± 0.02 mag for G006.9221-00.2513, 2.87 ± 0.18 mag for G007.0097-00.2542, 4.14 ± 0.03 mag for G006.9292-00.2460, and 4.79 ± 0.12 mag for G007.0574-00.2701.

(This table is available in its entirety in machine-readable form.)

As an alternative, we estimate the recovery rate of our sample against the one selected by Feigelson et al. (2013). They identified 41 Stage II/III and 22 Stage I YSOs having Spitzer photometry in all IRAC bands within the spatial boundary used in this work by modeling the available photometry against the YSO models of Robitaille et al. (2006). From their sample, we find that 28 Stage II/III and 11 Stage I YSOs have cross-matches in our final YSO sample. In their remaining Stage II/III sample, we find that two have MIR colors resembling PAH-contaminated sources, while two are likely stellar contaminants ([4.5]–[8.0] < 0.5) according to our analysis, and three had α values of Class II YSOs but were removed from the final sample based on their positions in the color–color plane resembling contaminants (see Section 3.2). The remaining six had α values between -1.7 and -2.1 (two of which fell in the contaminant region in the color–color plane). This distribution is expected given that the Stage and SED slope classifications are not analogous and depend on various factors (Robitaille et al. 2006). In addition, the Stage classification assumes that sources with $\alpha > -2$ are Stage II and sources with $\alpha < -2$ are Stage III. Out of the sample of 11 Stage I sources from Feigelson et al. (2013) not having counterparts in this sample, 1 star was not present in our source catalog, while 7 were discarded as PAH or shock emission contaminants. The three remaining sources have colors resembling reddened AGB stars and were removed from our final sample. Therefore, our sample compares well to the YSO catalog of Feigelson et al. (2013) once the constraints chosen in this work are applied.

Given the contamination rate and absence of a χ^2 fitting value (to adjudicate the quality of the classification) for the sources in Feigelson et al. (2013), archival infrared Class III sources from that catalog are not included here. Similarly, X-ray-bright Class III sources from that survey were not included, as the X-ray detection threshold chosen is considerably faint, and a significant fraction ($\sim$35%) of Class III X-ray sources do not have counterparts at other wavelengths, suggesting that they could be faint background sources. In addition, a distance value of 2700 pc (see Section 4.3) was used to calculate membership probabilities and absorption, possibly leading to the inclusion of more distant X-ray sources.

4. Pre-main sequence Stars

As YSOs evolve, their surrounding material collapses into circumstellar disks to conserve angular momentum. Accretion of mass from the disk toward the central stellar source via the stellar magnetosphere is necessary to gain enough material to initiate fusion. This accretion process results in a combination of unique signatures including excess ultraviolet continuum and line emission, notably in Hα (Gullbring et al. 1998). It is through this excess Hα emission that accreting young PMS stars can be readily identified.

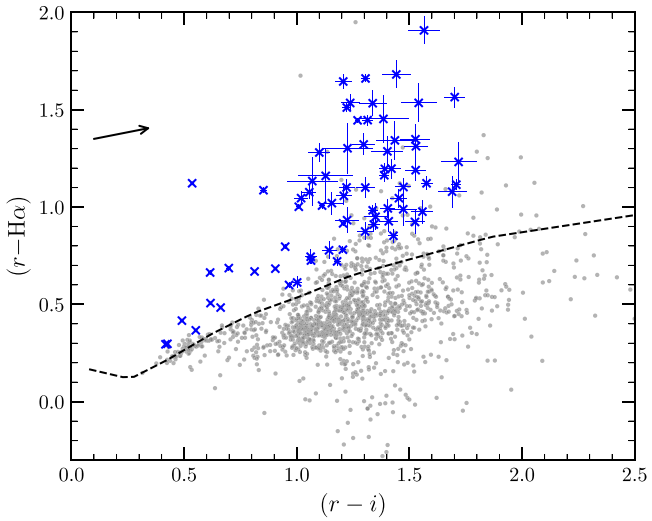

Figure 5. $(r-i)$ vs. $(r-\mathrm{H}\alpha)$ color–color diagram of all sources considered in the work, shown as circles. A reddening vector of 1 mag is shown in the upper left corner. The dashed line represents the main-sequence color locus calculated from the Pickles (1998) synthetic spectra, reddened by $A_V = 1.3$ mag. Stars selected as accretors based on the $\mathrm{EW}_{H\alpha}$ criterion are marked by blue crosses.

4.1. Identification of Accreting Pre-main sequence Stars Based on Photometric $EW_{\mathrm{H}\alpha}$

It has been established that the $(r-i)$ vs. $(r-\mathrm{H}\alpha)$ diagram (Figure 5) can be used to obtain estimates of the Hα equivalent width ($\mathrm{EW}_{H\alpha}$) of stars with precision photometry (De Marchi et al. 2010), given that the extinction and spectral type are relatively well approximated (to within 0.2 mag). We follow the method detailed in Kalari (2019) for VPHAS+ photometry to estimate the Hα equivalent width of all VPHAS+ sources, adopting the average absolute visual extinction value (A_V) of 1.3 mag from Rho et al. (2008).

From the values of photometrically estimated $\mathrm{EW}_{H\alpha}$, we select accreting PMS candidate stars based on their $(r-i)$ color (as a spectral type proxy). Note that $(r-i)$ colors and r-band magnitudes are corrected for Hα emission, as the Hα line falls within the r-band filter. Finally, images of accretors were also visually inspected using unsharp masking to remove sources

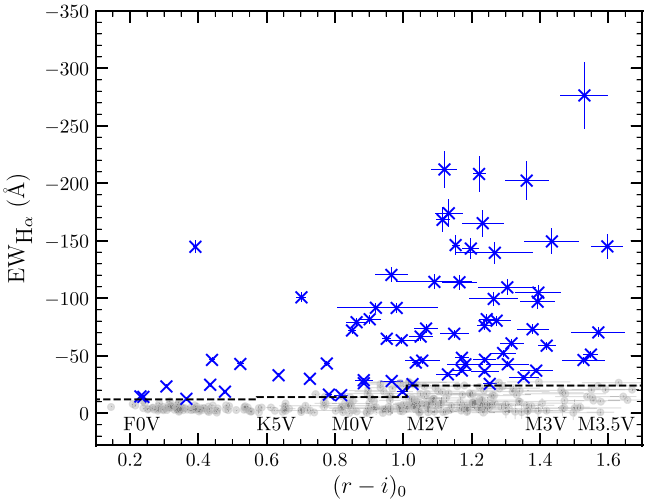

Figure 6. $(r-i)_0$ vs. EW$_{H\alpha}$ diagram of all sources. Stars selected as accretors are shown as blue crosses, along with their associated errors. The selection criteria are shown as a dashed line, and the spectral types at different values of $(r-i)_0$ are marked.

affected by nebulosity. The reader is referred to Kalari et al. (2015) for details on these procedures and also the Hα excess candidate selection criteria. To select PMS candidates, we use the spectral type−EW$_{H\alpha}$ criteria for classical T Tauri stars (CTTSs) of Barrado y Navascués & Martín (2003), adding to the upper limit of selected candidates based on the average error values of EW$_{H\alpha}$ (CTTSs are low-mass accreting PMS stars, showing Hα in emission). Stars earlier than K5 spectral type having EW$_{H\alpha}$ values less than −12 Å (where negative values denote in emission), stars in the K5−M2 spectral range with EW$_{H\alpha}$ values less than −15 Å, and stars later than M2 with Hα in emission less than −25 Å are selected as candidate PMS stars. Results of the selection procedure can be seen in Figure 6. The selection criteria account for propagated errors from the photometry and uncertainty in spectral type. They are also large enough to weed out main-sequence contaminants with solely chromospheric Hα emission. A total of 68 PMS candidates were selected based on this method. The resulting EW$_{H\alpha}$ values for the selected candidates, along with their photometry and astrometry, are given in Table 2.

4.2. Kinematic Properties of Pre-main sequence Candidates

Gaia proper motions provide a valuable membership indicator for nearby star-forming regions. Given that the Trifid Nebula is located in our line of sight toward the plane, it is likely that non-members may be erroneously identified as PMS members. Using proper motions, these can be excluded from further study.

M 20 is identified in the μ_α–μ_δ plane based on the mean motion of PMS candidates, having errors in any proper motion vector less than 0.5 mas yr^{-1}. The cluster itself is separated in proper motion space with respect to the surrounding field population, with an increase in density visible around the cluster center identified based on the motions of the PMS candidates (see Figure 7) and verified through the density map. Notice the large scatter of sources around the mean proper motion. This is expected given the location of the region in the Milky Way, as the photometry contains numerous background/foreground stars. The exact center of the region can be best distinguished using the identified PMS candidates.

To calculate the centroid in the proper motion plane, we fit double Gaussians to the proper-motion vector histograms, which represent a conflation of the field population, having a broad distribution, and the cluster population, which has a well-defined peak. The proper-motion centers in both directions were estimated based on the narrow Gaussian parameters. For μ_α, the center is 0.22 ± 0.8 mas yr^{-1}, and in μ_δ it is at -1.71 ± 1.6 mas yr^{-1}. The error bar denotes the width of the Gaussian peak.

Proper-motion candidates are selected based on the estimated proper-motion center of the cluster. We assume a median width of 2 mas yr^{-1} from the cluster center. PMS candidates meeting the proper-motion criteria are selected as those lying between $-1.8 < \mu_\alpha < 2.2$ and $-3.7 < \mu_\delta < 0.3$. Stars lying outside this bounding box are rejected as members, if their proper-motion values, along with the errors, lie outside this boundary. A total of 27 candidates were removed based on this criterion. Since the proper-motion center of the PMS members lies within the field proper-motion distribution, it is possible that some non-members may have been included in our final analysis.

Finally, non-accreting members that can potentially be identified using Gaia proper motions are not included, as the proper-motion distribution of the cluster overlaps significantly with the field. A selection criterion to isolate such stars using only proper motions would include a non-negligible fraction of non-members, with no further defining physical characteristic to identify members.

4.3. Distance to the Trifid Nebula

A large discrepancy exists in the literature on the distance toward M 20. Previous distance measurements have been made using spectroscopic parallax (Rho et al. 2008; Tapia et al. 2018) and extinction measurements (Cambrésy et al. 2011). Spectroscopic parallax measurements of HD 164492A place it at a distance between ∼1.6 and 2.0 kpc (Rho et al. 2008; Tapia et al. 2018), depending on the reddening law chosen (see Tapia et al. 2018). This places it behind the Sagittarius arm and in front of the Scutum arm of the Galaxy, whereas distance measurements using extinction mapping by Cambrésy et al. (2011) suggest a much farther distance of around 2.7 kpc, placing it firmly in the Scutum arm of the Galaxy. In this paper, we eschew depending on a priori knowledge of the reddening toward the region to measure the distances, by using high-fidelity parallax values of identified PMS candidates.

To estimate the distance toward the region, we consider only PMS candidates with Gaia EDR3 π errors (σ_π) less than 0.1 mas. As this criterion leaves us with only three stars, we add to the sample five previously identified members from the YSO sample, which all have $\sigma_\pi < 0.1$ mas. This increase from the IR-identified YSO sample is expected, as that sample is concentrated toward brighter magnitudes, where the σ_π are lower. In total, we have eight stars that are candidate members of the region, with high-fidelity π. Our chosen error criterion is to remove faint stars with non-negligible errors, which may degrade the accuracy and precision of the final distance estimate.

To estimate the individual distances of the chosen sample, we used the method of Bailer-Jones et al. (2018). An inference approach is adopted, which uses a prior with a length scale parameter (chosen here to be 1750 pc, based on the Galactic model given in Bailer-Jones et al. 2018). The resulting

Table 2
Optical Photometry, Gaia Astrometry, and Estimated Stellar Properties of Pre-main sequence Stars in the Trifid Nebula

VPHAS+ ID	r (mag)	i (mag)	Hα (mag)	EW$_{H\alpha}$ (Å)	μ_α (mas yr^{-1})	μ_δ (mas yr^{-1})	Mass ($M_\odot$)	Age (Myr)
816177248012	20.07 ± 0.07	18.53 ± 0.03	18.53 ± 0.06	-149.42 ± 11.1	-1.173 ± 0.678	-1.508 ± 0.412	$0.19^{+0.01}_{-0.02}$	$2.24^{+0.39}_{-0.44}$
816177242912	13.41 ± 0.01	12.99 ± 0.01	13.11 ± 0.01	-14.56 ± 1.5	-0.011 ± 0.596	-3.23 ± 0.433	$1.88^{+0.36}_{-0.23}$	$6.08^{+2.73}_{-3.00}$
816177256886	20.19 ± 0.07	18.47 ± 0.03	18.96 ± 0.07	-70.25 ± 4.1	0.522 ± 0.544	-0.522 ± 0.342	$0.18^{+0.01}_{-0.02}$	$1.81^{+0.28}_{-0.35}$
816856488067	19.55 ± 0.044	18.25 ± 0.025	18.23 ± 0.035	-113.88 ± 6.5	-0.667 ± 0.538	-2.75 ± 0.319	$0.25^{+0.01}_{-0.02}$	$3.01^{+0.68}_{-0.8}$
816856492037	19.87 ± 0.05	18.18 ± 0.02	18.79 ± 0.05	-46.22 ± 2.6	0.123 ± 0.529	-0.609 ± 0.313	$0.21^{+0.01}_{-0.01}$	$1.58^{+0.26}_{-0.37}$

Note. Five selected rows are shown to display the form and contents of the table. The full table is only available electronically, along with the source coordinates. Mass and age errors denote the upper and lower deviations based on the propagated photometric uncertainties, and assuming a distance and reddening uncertainty of 200 pc and 0.2 mag, respectively.

(This table is available in its entirety in machine-readable form.)

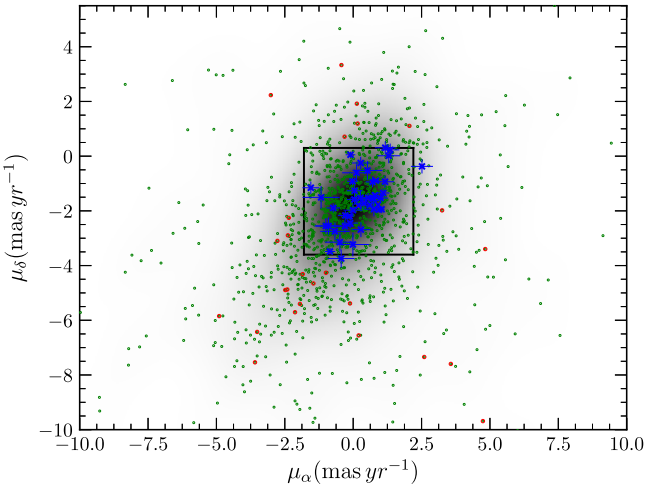

Figure 7. Gaia EDR3 proper motions of PMS candidates in the Trifid Nebula (green circles). The underlying inverted grayscale density map reflects the distribution of all Gaia sources in the field of view. Candidates selected as members on the basis of their proper motions are shown by blue crosses, while those rejected as members based on the proper motion criteria are shown as red circles. The proper-motion selection criteria are represented by the solid bounding box. Circles represent proper motions of all stars in the area of study.

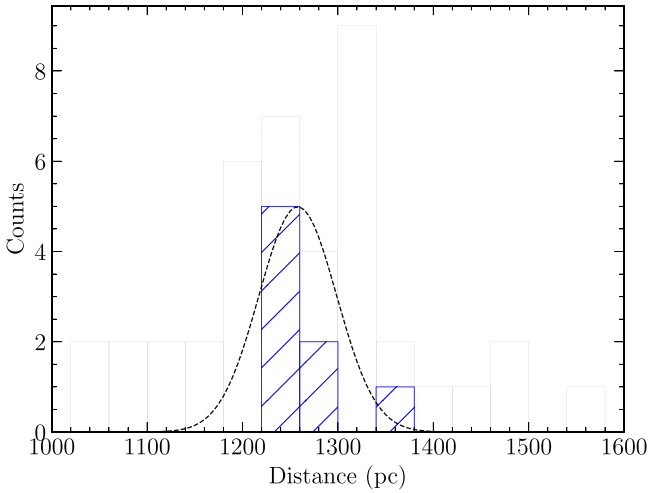

Figure 8. Histogram of distances of candidate members having $\sigma_\pi < 0.1$ mas (hatched bars). The resulting Gaussian is shown as a dashed line and has a peak of 1250 pc. Also shown only for comparison are the distances of all Gaia EDR3 sources meeting the proper-motion membership and parallax error criteria.

confidence intervals of the individual distances are asymmetric. Based on this method, the resulting distance histogram of all candidates is shown in Figure 8. An inverse weight of the mean error was applied to the histogram. A Gaussian is fit to the histogram, accounting for the well-defined cluster distance. From the peak of the Gaussian fit, we estimate a distance of 1257^{+190}_{-98} pc to M 20 (the median distance of the sample is 1255 pc). The distance toward the cluster is taken to be 1250 pc for our analysis. The asymmetric error represents the median of the 5th and 95th percentile confidence intervals of the resultant distance distribution.

The resulting distance from Gaia EDR3 parallaxes is much closer than previous measurements using spectroscopic parallaxes or extinction mapping. It agrees with the estimate of ~1.22 kpc made using Gaia DR2 parallaxes by Wade et al. (2017). As a comparison, also shown is the histogram of distances of Gaia EDR3 sources meeting the proper-motion criterion and having RUWE and σ_π within the limit for our sample. This sample has a median distance of 1300 pc but may contain few contaminant background stars. Finally, the new closer distance places the cluster firmly in the Sagittarius arm, alongside the star-forming regions in the near vicinity such as the Lagoon Nebula, Simeis 188 (both lying below the Galactic plane), and the optically invisible H II region W28 A2 and its supernova remnant W28.

4.4. Stellar Properties of Pre-main sequence Candidates

We estimate the stellar properties (mass M_* and age t_*) of the 41 PMS candidates that meet the proper-motion criteria, by interpolating their positions in the observed $(r-i)$ versus r color–magnitude diagram compared to model isochrones and mass tracks (Figure 9). The stellar isochrones and mass tracks of Bressan et al. (2012) in the VPHAS+ filter set (AB magnitude system) are utilized for this purpose. The AB to Vega offset values for the r- and i-band filters were 0.174 and 0.378, respectively. To understand the differences between the choice of stellar models, the M_* and t_* are compared to those estimated using the Siess et al. (2000) and Dotter et al. (2008) models in the VPHAS+ filter set. The metallicity in the models is set to solar, and the models only account for single stars. The A_V is assumed to be uniform and is set at 1.3 mag, with an R_V of 5.5 (Cambrésy et al. 2011) used to deredden the observed photometry. A distance of 1250 pc was used to transform the models to the observed distance. The results are reported in Table 2. Errors on the interpolated stellar properties include propagated photometric uncertainties and an assumed distance and extinction uncertainty of 200 pc and 0.2 mag, respectively.

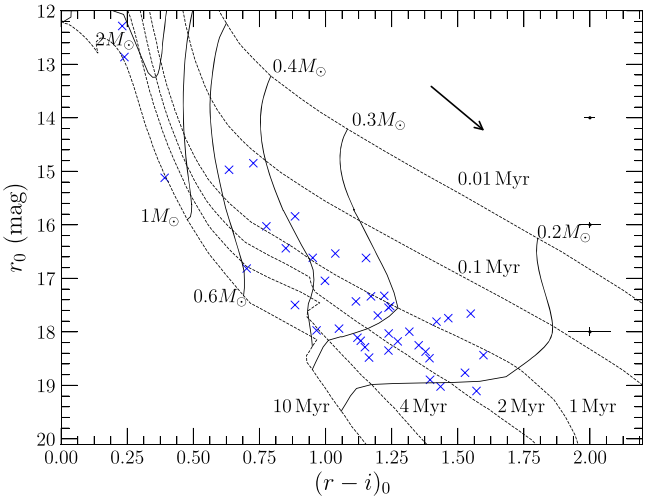

Figure 9. $(r-i)$ vs. r color–magnitude diagram of PMS candidates. Overplotted and labeled are the isochrones and mass tracks from Bressan et al. (2012). The extinction vector for $A_V = 1$ mag is shown in the upper right corner.

The effect of assuming a uniform extinction value on our results is also discussed.

The resulting color–magnitude diagram of the PMS stars, with the Bressan et al. (2012) stellar tracks and isochrones overlaid, is shown in Figure 9. PMS candidates from our sample fall approximately between the 0.2 and 2.0 $M_\odot$ tracks and are clustered between the 1 and 2 Myr isochrones. The results estimated from the three different stellar models are given in Figure 10. Here, the median mass of our candidates peaks around 0.3 $M_\odot$, with the most massive stars $\sim$2 $M_\odot$. This mass distribution is expected given the absolute r-band luminosity function of our candidates (Figure 10(c)), where our candidates fall between 2 and 9 mag (after correcting for extinction and distance). This approximates to early F to early M candidates, which corresponds to the derived mass range. Also marked for reference in Figure 10(c) are the expected absolute r-band magnitudes for main-sequence stars. There are no significant differences between stellar masses owing to the assumption of a particular set of models accounting for standard errors. Note that the mass of the most massive stars according to the Siess et al. (2000) models is slightly higher when compared to the other two model results.

The median age of the PMS candidates interpolated using the Bressan et al. (2012) isochrones is $1.5^{+0.3}_{-0.5}$ Myr. Error bars correspond to the median values for the upper and lower age errors, which are estimated from interpolated ages including the photometric, reddening, and distance uncertainties. The age distribution of the PMS candidates is shown in Figure 10(a). Note that the reddening vector exhibits a similar slope to the isochrones in the $(r-i)$ versus r plane (Figure 9). Minor increments in extinction will not change significantly the estimated age of the region, as evidenced by the resulting age errors. The median ages from the Bressan et al. (2012), Siess et al. (2000), and Dotter et al. (2008) models are 1.5, 1.4, and 1.9 Myr, respectively, and the estimated age differences between models are lower than the standard errors. For the remainder of this paper, we utilize the stellar properties derived using the Bressan et al. (2012) models.

The median age of the PMS stars estimated here ($\sim$1.5 Myr) is older than the literature age of the region $\sim$0.3 Myr. This age estimate was made based on the expected wind-bubble shell

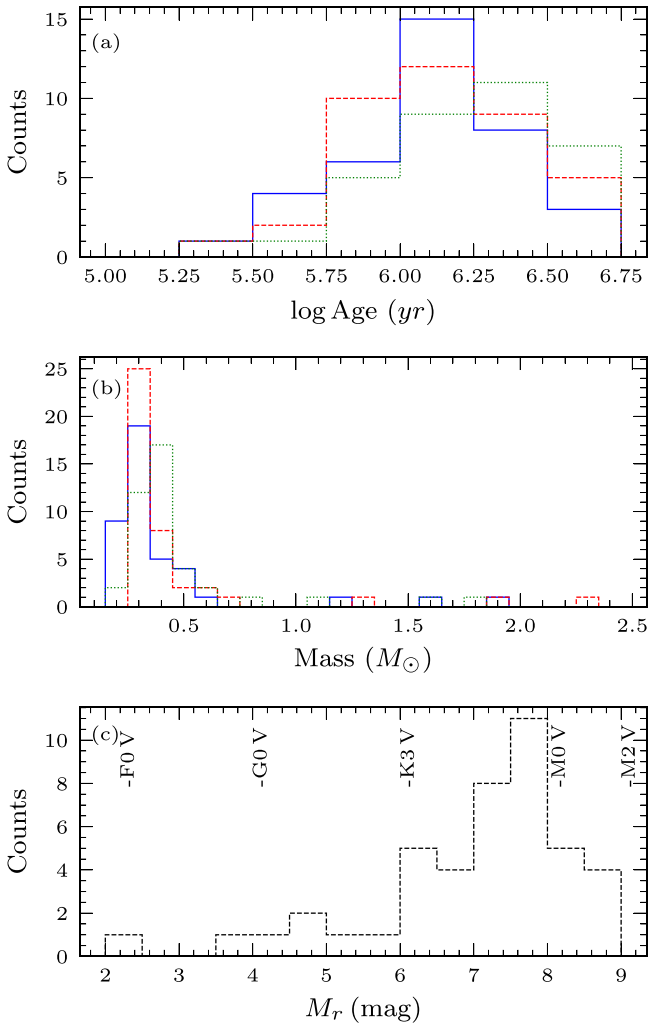

Figure 10. (a) Age, (b) mass, and (c) M_r-band histograms of PMS candidates in the Trifid Nebula. For the age and mass histograms, the solid (blue), dotted (green), and dashed (red) lines represent values estimated using the Bressan et al. (2012), Dotter et al. (2008), and Siess et al. (2000) models, respectively. In the M_r histogram the approximate absolute r-band magnitudes of select spectral types from Pecaut & Mamajek (2013) are labeled.

size by Cernicharo et al. (1998). Although this value does not take into account earlier stages, it represents a good lower limit to the cluster age. The photoionization time of cometary globules in the region (Lefloch et al. 2002) and the presence of dense star-forming cores (Tapia et al. 2018) attest to the most recent burst of star formation in the region (Rho et al. 2008), $<\sim$1 Myr ago. The age estimated in this work represents well only the current generation of PMS stars in the region. This generation of stars must have formed alongside or slightly before HD 164492A, as its spectroscopic age is around 0.6 Myr (Petit et al. 2019).

The impact of our assumption of a uniform extinction value $A_V = 1.3$ mag on our resultant ages is tested by adopting higher uniform values of extinction. Assuming $A_V = 2$ mag increases the median age of the sample slightly to $\sim$1.8 Myr. This agrees with the expectation of the reddening vector discussed earlier. Assuming a higher extinction of $A_V = 5$ mag, around 10 stars fall beyond the 100 Myr isochrone, and their ages cannot be estimated. These stars would be considerably blue and lie beyond the main sequence at the distance of 1250 pc. The median age of the remaining sample is 2.8 Myr. Thus, it is

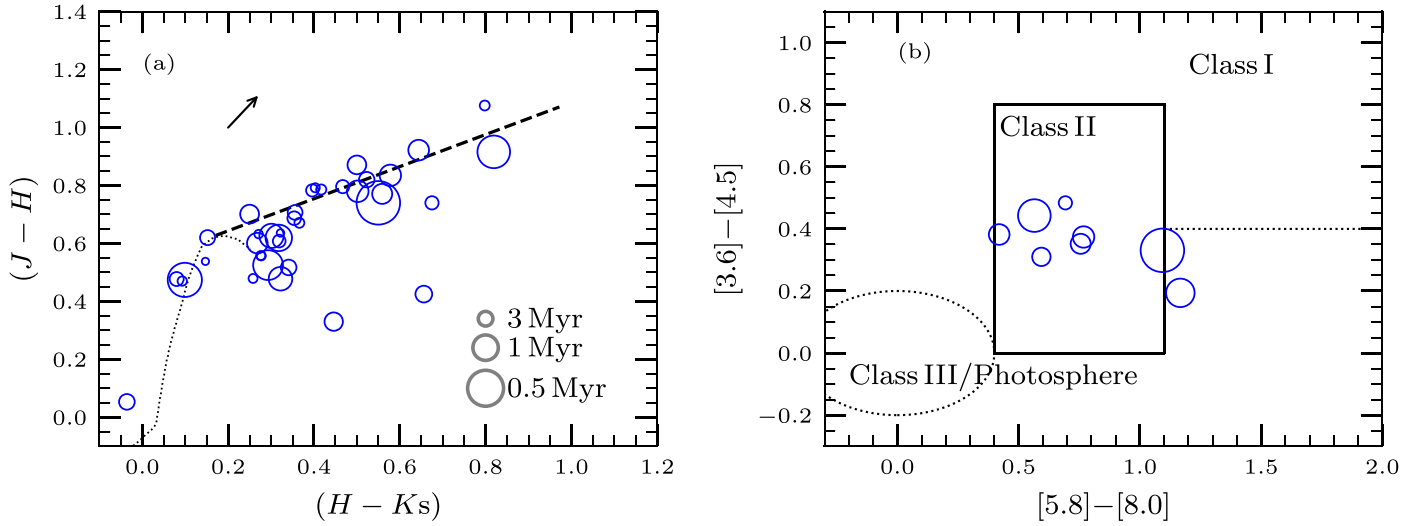

Figure 11. (a) ($H-Ks$) vs. ($J-H$) color–color diagram of the PMS sample. The reddening vector for $A_V = 1$ mag is also shown in the upper left corner. The CTTS locus from Meyer et al. (1997) is shown as a dashed line. The main-sequence colors from Pecaut & Mamajek (2013) are shown by a dotted line. (b) The MIR colors of the sample are shown. The boundary of colors for Class II sources with a median accretion of $10^{-8}\,M_{\odot}\,\mathrm{yr}^{-1}$ from the models of D'Alessio et al. (2001) is shown, along with the positions of Class I and Class III sources. In both panels, the size of the symbol is scaled with the estimated stellar age, given in the index in the lower right corner of panel (a).

likely that the PMS stars have a lower mean extinction than assumed here, rather than higher. Finally, we found that a simulation of the random variation of individual stellar reddening for PMS stars leads to an age estimate of 1.7 Myr. To arrive at this value, we generated random values for the assumed extinction correction (between $A_V = 0.5$ and 5 mag) for each star. Each star was also cloned 10,000 times, and the median age of these clones with random extinction correction was the result. These experiments serve to demonstrate that the assumed mean extinction is not a significant underestimation for the majority of our sample, and that while individual stellar extinction values are essential for a precise age estimate, the final median age of our sample should not vary significantly. From this analysis, we also suggest that future spectroscopic surveys of the young stellar population that can estimate precise individual extinctions and spectroscopic properties can pin down the precise age of individual stars in the Trifid Nebula.

4.5. Infrared Properties of Pre-main sequence Candidates

As described in Section 3, circumstellar disks surrounding PMS stars are heated by the central star. This leads to an inner disk wall that reradiates and absorbs energy primarily at NIR wavelengths, leading to prominent K-band excesses compared to main-sequence stars. Evidence for NIR–MIR excesses in PMS stars is thus an excellent independent indicator of circumstellar disks and accretion. The exact value of the IR excesses depends on many factors (Meyer et al. 1997). Note that an absence of excess does not conclusively rule out the presence of a circumstellar disk but could be due to an inner disk hole or edge-on disk inclination angle.

To identify whether our candidate PMS stars have NIR or MIR excesses resembling circumstellar disks, we use the cross-matched NIR and MIR data described in Section 2.4. A total of 39 PMS candidates have NIR counterparts in *JHKs* bands from the UKIDSS survey meeting the photometric criteria. The ($H-Ks$) versus ($J-H$) color–color diagram is shown in Figure 11(a). The main-sequence locus from Pecaut & Mamajek (2013) is shown along with the extinction vector for 1 mag. Also marked is the CTTS locus from Meyer et al. (1997), showing the expected NIR excesses for CTTS stars having accretion rates between 10^6 and $10^8\,M_{\odot}\,\mathrm{yr}^{-1}$. A total of 90% of our sample has colors within errors falling on the CTTS locus, suggestive that the majority of our sample has circumstellar disks. The lack of NIR excesses for a few stars in our sample does not suggest the absence of circumstellar disks and could be due to inclination angle or inner disk hole.

While 32 PMS candidates have counterparts in one or more MIR Spitzer bands, only eight have photometry in all bands and are shown in Figure 11(b). Seven are marked as Class II YSOs from the α analysis (with the remaining star having $\alpha = -1.9$). For the GLIMPSE survey, the limiting magnitude in the Spitzer [3.6] band is around 14 mag, which is approximately a mid-K spectral type. Therefore, it is not surprising that while nearly all our candidates have NIR counterparts with high-quality photometry from UKIDSS, only a brighter subsample have MIR photometry. The expected colors for stars having mean accretion rates of $10^{-8}\,M_{\odot}\,\mathrm{yr}^{-1}$ from D'Alessio et al. (2001) are shown, along with the expected positions of Class I and Class III sources. All of the sample falls in the expected positions for Class II sources with the mean accretion rate around $10^{-8}\,M_{\odot}\,\mathrm{yr}^{-1}$. The NIR and MIR colors of our sample clearly suggest that they are PMS stars. The IR color–color diagrams shown in Figure 11 also relate the position in color space to the estimated age. No clearly demarcated trend is seen from the observed colors. Stars that are detected at MIR wavelengths are younger than the general sample. The photometry of the PMS sample in NIR and MIR is given in Table 2.

4.6. Sample Completeness

Sample completeness is a function of photometry meeting our quality criterion for all sources in the Trifid Nebula in magnitude and spatial location. Completenesses in magnitude space estimated from the luminosity function in *ri*Hα are 19.8, 18.5, and 19.4 mag, respectively (see Kalari et al. 2015 for

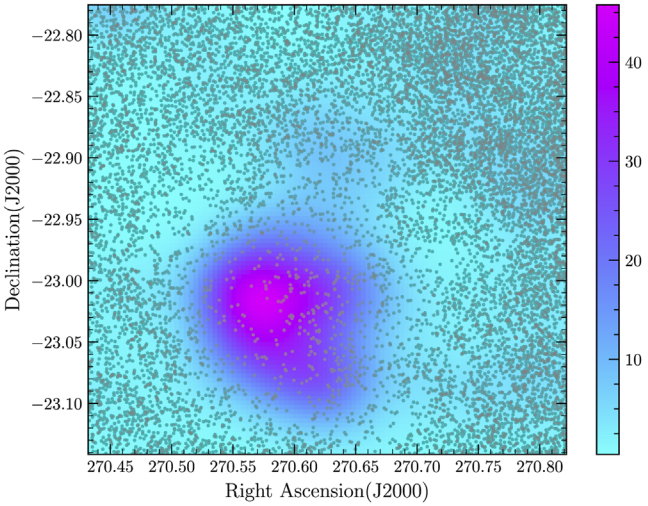

Figure 12. Color map in right ascension and declination depicting ratio of sources detected to those whose photometry is affected by spatially varying nebulosity on small scales. Gaia EDR3 sources are overlaid as gray circles.

details). Based on the photometric magnitudes, we are complete until a stellar mass around 0.45 $M_{\odot}$. Spatial variation of completeness is considerable in our sample owing to nebulosity varying on small spatial scales. In this scenario, high-fidelity photometry of sources cannot be determined using currently available sky subtraction techniques (see Section 2.2). Note that while these sources are identified, their photometry, particularly in Hα, is sufficiently degraded to be unsuitable for further analysis. To gauge this incompleteness, we estimate the fraction of the total number of sources detected in the *ri*Hα magnitude across the spatial extent of the study to the number of sources meeting the photometric quality criteria in equally spaced grids. This fraction is represented in Figure 12. This is created by assuming that, for an increasing aperture radius, if the increase in observed magnitude is larger than the error on the magnitudes, the photometry is affected by the increasing nebulosity (i.e., being classed as an extended source in Drew et al. 2014). This is given by the equation

$$|r_4 - r_3| > 3 \times \sqrt{{r_4}^2 + {r_3}^2} + 0.05. \quad (2)$$

Here r_4 and r_3 represent the magnitudes in apertures of 2.″8 and 2″, respectively. The smoothed density map of sources affected by nebular subtraction in Figure 12 suggests that the sample is more incomplete toward the central dust lane and HD 164492A. Accounting for the missing fraction of PMS stars due to this spatial incompleteness is difficult, as it depends on the inherent spatial distribution and their fraction compared to the total number of sources in a given region. This caveat is considered when analyzing the spatial distribution in the Trifid Nebula in the region around HD 164492A. Also overplotted in Figure 12 is the spatial distribution of Gaia EDR3 point sources, as a comparative reference for high-quality optical imaging in the region.

Overall, we can conclude that our sample is complete down to masses of 0.45 $M_{\odot}$, and spatially our sample is significantly affected by the nebulosity. The effect of this incompleteness suggests sources missing around the central dust lane and near HD 164492A. Based on this, we can assume that our sample represents only a lower limit of PMS stars around HD 164492A. Given these circumstances, we define a radius around the central O star where the sample is incomplete and consider this caveat when discussing the spatial properties of the PMS sample.

5. Discussion

5.1. Star Formation Triggered by CCC

As discussed in Section 1, the Trifid Nebula is a proposed site of CCC triggering star formation. From a submillimeter study of CO lines Torii et al. (2011, 2017) identified three distinct velocity components at 1.4, 9 (hereafter 2 km s^{-1} cloud and cloud C, respectively, following their nomenclature), and 18.2 km s^{-1}, representing three different molecular clouds. They claimed that the 2 km s^{-1} cloud and cloud C are observed to have higher temperatures and are likely heated by the central ionizing source (HD 164492A) based on positional and luminosity arguments–suggesting that they are the parent clouds of the central cluster (while the 18 km s^{-1} cloud is unlikely to be related to current star formation in the region). Torii et al. (2011) indicate that the observed velocity pattern is systemic. The 2 km s^{-1} cloud is currently moving toward us, with cloud C moving away from us with an observed velocity separation of 7.5 km s^{-1}. Here, the velocity separation refers to the differences in the peak velocity of the two clouds' CO spectra and is taken from Torii et al. (2011). The 2 km s^{-1} cloud is associated with the dark lanes in the Trifid Nebula, but cloud C does not correspond to the optically observed features strengthening the argument that cloud C lies behind the 2 km s^{-1} cloud in our line of sight. The total estimated molecular and stellar mass is insufficient to gravitationally bind the system, leading the authors to propose a different mode of star formation. They suggest that a consistent scenario with the observed velocity and spatial properties of the molecular clouds is that these two clouds collided ∼1 Myr ago, with the observed relative velocity difference arising from the collision (see also Figure 13). The collision between these two clouds triggered rapid star formation at the location of the collision, including the formation of HD 164492A.

Important differences between stars forming in a single molecular cloud and a pair of colliding clouds are the spatial positions and age spreads of the newly formed stars with respect to the position and velocities of their natal molecular clouds (Loren 1976). When gravitational collapse of molecular clouds is induced by turbulence, it is thought that heavier filaments fall toward the center, and the majority of stars in the central region form over a prolonged period of time from such dense material, giving rise to a concentration of young stars in cluster centers, with the more massive stars forming there preferentially. Older stars are expected to be detected more toward the outskirts of regions, either due to lower molecular densities in the outer areas, resulting in the earliest period of star formation exhausting material to form stars, or due to dynamical interactions over time. In the case of head-on CCC as considered in M 20, the new generation of stars will form where the densities and compression are the highest. This is expected to be toward the edges of the collided clouds, as a cavity is created toward the center of the collision, along with a detected bridge feature at intermediate velocities (Torii et al. 2017). The stars that formed rapidly after the collision will now be found in a region where the two separate velocity components are coalescing into one intermediate velocity. The younger generation of star formation currently occurring

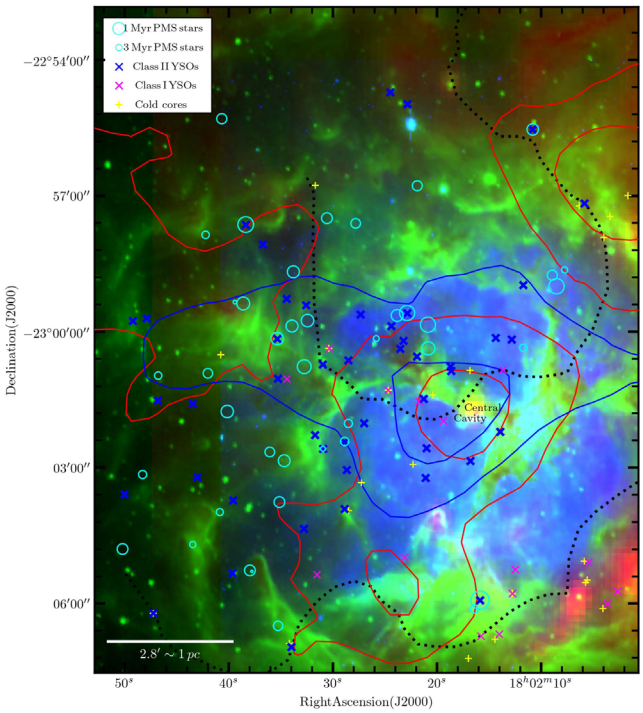

Figure 13. Herschel 350 μm/8 μm Spitzer/VPHAS+ Hα *rgb* image of the Trifid Nebula. North is up and east is left. The scale bar corresponding to 1 pc at the distance of the Trifid Nebula is also given. Circles mark the location of PMS stars detected in our sample. Their size is related to their age and scaled according to the legend in the upper left corner. Blue and cyan crosses mark the position of Class II and Class I sources, respectively, while the plus sign indicates the location of star-forming cores from Tapia et al. (2018). The blue and red contours indicate the blueshifted 2 km s^{-1} cloud and redshifted cloud C, which have collided following Torii et al. (2011). The contour levels are drawn for clarity at 18 and 36 K km s^{-1} for both clouds. Black contours represent the filaments identified from Herschel imaging.

will be concentrated toward the edges of the collided clouds and near the edges of the cavity, where dense molecular material is not yet exhausted. Stars formed as a result of the collision will be found exclusively around the collapsing region, but the central overlapping region where the clouds collided might be devoid of stars.

Therefore, the spatial and age spreads of young stars can be correlated with the velocity and spatial properties of molecular clouds and filaments to identify the sites of CCC induced star formation. Based on the demographics of the young stellar population identified in Sections 3 and 4, we explore here whether they provide evidence for or against the CCC hypothesis.

5.1.1. State of Colliding Clouds in Trifid Nebula

The mass of the two clouds is calculated based on the CO luminosities and line widths reported in Torii et al. (2011), where the authors adopted the $X_{\rm CO}$ factor of 2.0×10^{20} cm^{-2}(K km s^{-1})$^{-1}$ to convert the CO luminosity to mass. The difference between the calculations reported here and those in Torii et al. (2011) is in the distance adopted. For the calculations reported in this paper the distance adopted is 1250 pc from Gaia EDR3 parallaxes, whereas Torii et al. (2011) adopted much larger distance estimates of 1700 and 2700 pc. Based on the new distance, the total mass and radius of cloud C are estimated as 0.5×10^3 $M_\odot$ and 0.9 pc, respectively. The 2 km s^{-1} cloud has a mass of 0.35×10^3 $M_\odot$ and a radius of 0.7 pc. Considering the gravitational situation of the cloud, we can calculate whether it is bound or unbound based on the $\alpha_{\rm G}$ parameter. If $\alpha_{\rm G} > 1$, the cloud is considered unbound, and if $\alpha_{\rm G} < 1$, the cloud is bound. Here,

$$\alpha_{\rm G} = \frac{5\sigma_v R}{GM}. \quad (3)$$

The projected distance and velocity separation (the actual observed separation may be higher depending on the inclination angle) between the clouds are denoted by R and σ_v respectively. From Torii et al. (2011), we adopt σ_v of 7.5 km s^{-1} and R of 1–2 pc. From this, we estimate that the mass M required to bind the clouds is $\sim 10^4$ $M_\odot$, an order of magnitude higher than both the stellar and cloud masses combined (Torii et al. 2011). Hence, the clouds can be considered to be gravitationally unbound. Based on their velocity difference, they are expanding away from each other. Note that Torii et al. (2011) arrived at a very similar conclusion, albeit for a slightly higher distance estimate. Similarly, Torii et al. (2011) calculated that the mechanical luminosity generated by the stellar wind of HD 164492A is insufficient to cause the observed cloud expansion. Therefore, we can conclude similar to Torii et al. (2011) that the two molecular clouds are expanding away from each other and are not gravitationally bound, and the observed cloud velocities must be systemic. Based on the present direction of the velocities and the cloud size, the two clouds must have collided $\sim$0.7 Myr ago (Torii et al. 2011), not accounting for projection effects. This value may vary based on projection effects by a factor of 2.

The dynamical age ($t_{\rm dyn}$) of the H II region encompassing the Trifid Nebula is estimated as follows:

$$t_{\rm dyn} = \frac{4R_s}{7c_s}\left[\left(\frac{R_{\rm H\,II}}{R_s}\right)^{(7/4)} - 1\right]. \quad (4)$$

Here R_s is the radius of the Strömgren sphere, $R_{\rm H\,II}$ is the radius of the Trifid Nebula, and c_s is the sound speed. R_s is also calculated following Equation (1) in Tremblin et al. (2014). To calculate R_s, a recombination coefficient of 3×10^{-13} cm^3 s^{-1} (adopting a temperature of 8000 K) and a density of 3400 cm^{-3} are assumed from Tremblin et al. (2014), as they best represent the solar neighborhood. We also adopt the ionizing flux from Smith et al. (2002) for the central O7.5V star to be 5×10^{48} photons s^{-1}. Differences in the assumptions of mean density can critically change the dynamical age (e.g., Tremblin et al. 2014), so we calculate errors bars on our sample assuming a mean density range of 1000–10,000 cm^{-3} . From Figure 1, we estimate $R_{\rm H\,II} \sim 2.5$ pc, assuming a distance of 1250 pc. The resulting dynamical age is $\sim 0.85^{+0.15}_{-0.45}$ Myr. This is larger than the estimate of 0.3 Myr arrived at by Cernicharo et al. (1998), assuming a distance of 1680 pc and density of 1000 cm^{-3}. The value reported is in agreement with the spectroscopic age of HD 164492A ($\sim$0.6 Myr).

5.1.2. Filamentary Structure

Long-wavelength images of the Trifid Nebula taken from the Herschel space telescope display long filamentary structures. These structures can be identified and extracted using various

decomposition algorithms. To identify the filamentary structures visible in the 500 μm Herschel image of the Trifid Nebula, we utilize the FilFinder algorithm from Koch & Rosolowsky (2015). The "filaments" are identified from a flattened and masked image to remove bright compact sources and pick out the filamentary structure. The size threshold for masking chosen was experimented with to better highlight the small scale and faint regions when visually comparing to the flattened image, and a value of 600 was used. The final pruned skeletons representing the "filaments" are shown in Figure 13. From the image, we identified two filaments in the Trifid Nebula. The two structures do not correspond visually to the optical nebulosity and the three visible dust lanes. The filaments run along the visible emission in the MIR emission but do not intersect.

A clear distinction can be made between the two filaments in terms of the young stellar population. Along the northern filament lies the bulk of the Class II YSO and PMS population detected, while only three fall along the southern filament. The southern filament, especially toward the southwest edge, falls across a clump of cold cores identified by Lefloch et al. (2002) and a grouping of Class I YSOs. This suggests that stars forming along the southern filament must be younger than the bulk of the stellar population identified lying along the northern filament given the relative ratio of PMS stars and Class II YSOs to Class I YSOs and cold cores.

5.1.3. Spatial Distribution and Star Formation Chronology of YSOs and Accreting PMS Stars

The mean ages of the Class II YSOs are assumed to be similar to or slightly younger than the accreting PMS stars, whose median age is 1.5 Myr. The Class I YSOs are considered to be much younger (Harvey et al. 2006), around $\sim$0.5 Myr. The dynamical age of the region ($\sim$0.85 Myr) is larger than the estimated age of the Class II YSOs, with the former specifying a lower limit to the age of the region. Further precise estimates of the reddening and distance may verify the ages of the accreting PMS stars and Class II YSOs (see Section 4.4). An additional timescale in consideration here is the crossing time. Following Adamo et al. (2020), and assuming a total stellar mass of 500 $M_{\odot}$ based on Torii et al. (2011), the crossing time estimated is $\sim$2.7 Myr. This is 2σ larger than the median age of the accreting PMS stars. Future spectroscopy of cluster members that can estimate the radial velocity spread of the region is essential to confirm the crossing time (Adamo et al. 2020).

Figure 13 shows the positions of the accreting PMS stars, YSOs, and cold cores detected by Tapia et al. (2018) in the Trifid Nebula. They are expected to represent an age sequence of oldest to youngest stars currently forming in M 20. These positions are overlaid on the Hα VPHAS+ image, the Spitzer 8 μm image, and the Herschel 350 μm, respectively, for the reader to relatively gauge the position of the Hα nebulosity and the PAH and IR emission. Also shown are the 2 km s^{-1} and cloud C contours taken from Torii et al. (2011). The approximate location of the central cavity is also given and corresponds to the complementary distribution region in Torii et al. (2017) in the range of $18^{h}02^{m}15^{s}$–19^{s} and $-23°03'$–$01'$. The boundaries of the molecular clouds can be visualized by the respective cloud contours given in Figure 13.

From Figure 13 the positions of the accreting PMS stars and YSOs are seen to correlate to the positions of the molecular clouds. The PMS stars and Class II YSOs are preferentially found along the boundaries of the molecular clouds, with none found within the boundaries of the central cavity. Class II YSOs are also located along the edges of the dust lanes. Further, the ages of the stars show no clear demarcation between old or young stars, besides a group of older stars lying outside the displayed boundaries of the molecular clouds to the southeast. The absence of PMS stars near the center is not decisive evidence, as the PMS sample is incomplete spatially. However, also no Class II YSOs are detected toward the center of the nebula. This can be considered as evidence that the Spitzer photometry is not affected toward the central region when compared to the optical photometry.

In contrast, the Class I YSOs are found favoring the dust lanes near the center of the nebula. In addition, a concentration of Class I YSOs and cold cores is found toward the southwest, outside clearly visible nebulosity in Hα, but near nebulous filaments visible in the 8 μm image. This suggests that a newer generation of stars is being formed near the periphery, where the cold cores and the Class I sources are located. A single flat source is detected toward the central region, and a few Class I sources and the cold core TC1 are found near HD 164992A.

From the ages and positions of the PMS stars, YSOs, and cold core samples compared to the colliding molecular clouds in Figure 13, there is evidence suggestive of CCC induced star formation. The locations of the stars are along the edges of the two clouds with similar ages. This age is smaller than the crossing timescale $\sim$2.7 Myr. No stars are found near the center of the two colliding clouds, suggestive of a cavity devoid of ongoing star formation. The PMS stars and Class II YSOs have ages $\sim$1.5 Myr. Note that a small grouping of Class I YSOs and cold cores to the southwest of the nebula falling on the southern filament are younger than most of the stellar population in the region and are forming in a subsequent outburst of star formation.

In summary, the gravitational energy of the clouds is not sufficient to bind them, and the heating from HD 164492A seems insufficient to cause the observed expansion. The velocity differences between the two clouds are systematic. Traveling backward, they must have collided $\sim$0.7 Myr. The collision of the small cloud created a cavity on the larger cloud where the two clouds collide and now overlap in the projected space (Torii et al. 2017). Star formation was triggered likely immediately after, and molecular material across the two clouds collapsed to form the currently visible young stellar population roughly a million years ago. The positions and ages of YSOs and PMS stars lend credence to the hypothesis that they may have formed after CCC. The Class II YSOs and PMS stars ($\sim$1.5 Myr) are located preferentially toward the edges of the clouds and not found in the center. Class I YSOs ($\lesssim$0.5 Myr) are found more concentrated around the center of the clouds. The stars on either ends of the molecular cloud are around the same age, which is less than the crossing time of $\sim$2.7 Myr.

A tightness in the dynamical age (0.85 Myr) and the age of the accreting PMS stars may be alleviated if there are precise reddening and distance estimates. Further spectroscopic observations are needed to confirm this. Such spectroscopic observations can also potentially identify diskless/non-accreting members. While the ages of such members are in keeping with the general age of the region they reside in, they are often

spatially less concentrated (although occupying similar spatial distributions) compared to their more active brethren.

6. Conclusions

1. We have identified 46 Class II, 9 Flat, and 6 Class I YSOs in the Trifid Nebula on the basis of their infrared SED slope, α, and positions in the MIR color–color plane. No Class III YSOs are included in our analysis.
2. A total of 41 accreting PMS stars were identified on the basis of Hα excess against *ri*Hα photometry. The identified stars have proper motions indicating that they likely belong to the Trifid Nebula. A total of 90% of the accreting PMS stars have NIR colors, indicating the presence of a circumstellar dust disk.
3. The distance to the Trifid Nebula measured from Gaia EDR3 parallaxes of a subset of cluster members is around 1250 pc, placing the region in the Sagittarius arm of the Milky Way.
4. Based on the positions and ages of the young stellar population in the region, it is likely that star formation was triggered by the collision of two clouds $\sim$1 Myr ago, leading to the currently observed distribution.

V.M.K. acknowledges funding from CONICYT Programa de Astronomia Fondo Gemini-Conicyt No. 32RF180005. The work of V.M.K. is supported by NOIRLab, which is managed by the Association of Universities for Research in Astronomy (AURA) under a cooperative agreement with the National Science Foundation. V.M.K. thanks K. Torii for kindly providing the molecular cloud cubes and the anonymous referee for detailed comments that helped improve this paper. This work is based in part on observations made with the Spitzer Space Telescope, which is operated by the Jet Propulsion Laboratory, California Institute of Technology, under a contract with NASA. This work is based in part on data obtained as part of the UKIRT Infrared Deep Sky Survey. Based in part on observations made with ESO Telescopes at the La Silla or Paranal Observatories under program ID(s) 177.D-3023(B), 177.D-3023(C), 177.D-3023(D), 177.D-3023(E). This work presents in part results from the European Space Agency (ESA) space mission Gaia. Gaia data are being processed by the Gaia Data Processing and Analysis Consortium (DPAC). Funding for the DPAC is provided by national institutions, in particular the institutions participating in the Gaia MultiLateral Agreement (MLA). Herschel is an ESA space observatory with science instruments provided by European-led Principal Investigator consortia and with important participation from NASA.

Facilities: Spitzer, Herschel, VLT(VST), Gaia.

Software: APLpy (Robitaille & Bressert 2012), FILFinder (Koch & Rosolowsky 2015).

ORCID iDs

Venu M. Kalari https://orcid.org/0000-0002-4641-2532

References

Adamo, A., Zeidler, P., Kruijssen, J. M. D., et al. 2020, SSRv, 216, 69
Allen, L. E., Calvet, N., D'Alessio, P., et al. 2004, ApJS, 154, 363
Bailer-Jones, C. A. L., Rybizki, J., Fouesneau, M., Mantelet, G., & Andrae, R. 2018, AJ, 156, 58
Barrado y Navascués, D., & Martín, E. L. 2003, AJ, 126, 2997
Benjamin, R. A., Churchwell, E., Babler, B. L., et al. 2003, PASP, 115, 953
Bressan, A., Marigo, P., Girardi, L., et al. 2012, MNRAS, 427, 127
Cambrésy, L., Rho, J., Marshall, D. J., & Reach, W. T. 2011, A&A, 527, A141
Cernicharo, J., Lefloch, B., Cox, P., et al. 1998, Sci, 282, 462
Cutri, R. M., Skrutskie, M. F., van Dyk, S., et al. 2003, 2MASS All Sky Point Source Catalog, NASA/IPAC Infrared Science Archive
D'Alessio, P., Calvet, N., & Hartmann, L. 2001, ApJ, 553, 321
De Marchi, G., Panagia, N., & Romaniello, M. 2010, ApJ, 715, 1
Dotter, A., Chaboyer, B., Jevremović, D., et al. 2008, ApJS, 178, 89
Drew, J. E., Gonzalez-Solares, E., Greimel, R., et al. 2014, MNRAS, 440, 2036
Feigelson, E. D., Townsley, L. K., Broos, P. S., et al. 2013, ApJS, 209, 26
Fukui, Y., Habe, A., Inoue, T., Enokiya, R., & Tachihara, K. 2021, PASJ, 73, S1
Gaia Collaboration, Brown, A. G. A., Vallenari, A., et al. 2020, A&A, 649, A1
Gullbring, E., Hartmann, L., Briceno, C., & Calvet, N. 1998, ApJ, 492, 323
Gutermuth, R. A., Megeath, S. T., Myers, P. C., et al. 2009, ApJS, 184, 18
Harvey, P. M., Chapman, N., Lai, S.-P., Evans, N. J. I., et al. 2006, ApJ, 644, 307
Indebetouw, R., Mathis, J. S., Babler, B. L., et al. 2005, ApJ, 619, 931
Kalari, V. M. 2019, MNRAS, 484, 5102
Kalari, V. M., Vink, J. S., Drew, J. E., et al. 2015, MNRAS, 453, 1026
Koch, E. W., & Rosolowsky, E. W. 2015, MNRAS, 452, 3435
Lefloch, B., Cernicharo, J., Rodríguez, L. F., et al. 2002, ApJ, 581, 335
Loren, R. B. 1976, ApJ, 209, 466
Lucas, P. W., Hoare, M. G., Longmore, A., et al. 2008, MNRAS, 391, 136
McKee, C. F., & Ostriker, E. C. 2007, ARA&A, 45, 565
Megeath, S. T., Allen, L. E., Gutermuth, R. A., et al. 2004, ApJS, 154, 367
Meyer, M. R., Calvet, N., & Hillenbrand, L. A. 1997, AJ, 114, 288
Pecaut, M. J., & Mamajek, E. E. 2013, ApJS, 208, 9
Petit, V., Wade, G. A., Schneider, F. R. N., et al. 2019, MNRAS, 489, 5669
Pickles, A. J. 1998, PASP, 110, 863
Rho, J., Corcoran, M. F., Chu, Y.-H., & Reach, W. T. 2001, ApJ, 562, 446
Rho, J., Lefloch, B., Reach, W. T., & Cernicharo, J. 2008, in M20: Star Formation in a Young HII Region, ed. B. Reipurth, Vol. 5 (San Francisco, CA: ASP), 509
Rho, J., Reach, W. T., Lefloch, B., & Fazio, G. G. 2006, ApJ, 643, 965
Robitaille, T., & Bressert, E. 2012, APLpy: Astronomical Plotting Library in Python ascl:1208.017, Astrophysics Source Code Library
Robitaille, T. P., Whitney, B. A., Indebetouw, R., Wood, K., & Denzmore, P. 2006, ApJS, 167, 256
Siess, L., Dufour, E., & Forestini, M. 2000, A&A, 358, 593
Smith, L. J., Norris, R. P. F., & Crowther, P. A. 2002, MNRAS, 337, 1309
Tapia, M., Persi, P., Román-Zúñiga, C., et al. 2018, MNRAS, 475, 3029
Torii, K., Enokiya, R., Sano, H., et al. 2011, ApJ, 738, 46
Torii, K., Hattori, Y., Hasegawa, K., et al. 2017, ApJ, 835, 142
Tremblin, P., Anderson, L. D., Didelon, P., et al. 2014, A&A, 568, A4
Urquhart, J. S., Csengeri, T., Wyrowski, F., et al. 2014, A&A, 568, A41
Wade, G. A., Shultz, M., Sikora, J., et al. 2017, MNRAS, 465, 2517
Yusef-Zadeh, F., Biretta, J., & Geballe, T. R. 2005, AJ, 130, 1171
Yusef-Zadeh, F., Shure, M., Wardle, M., & Kassim, N. 2000, ApJ, 540, 842